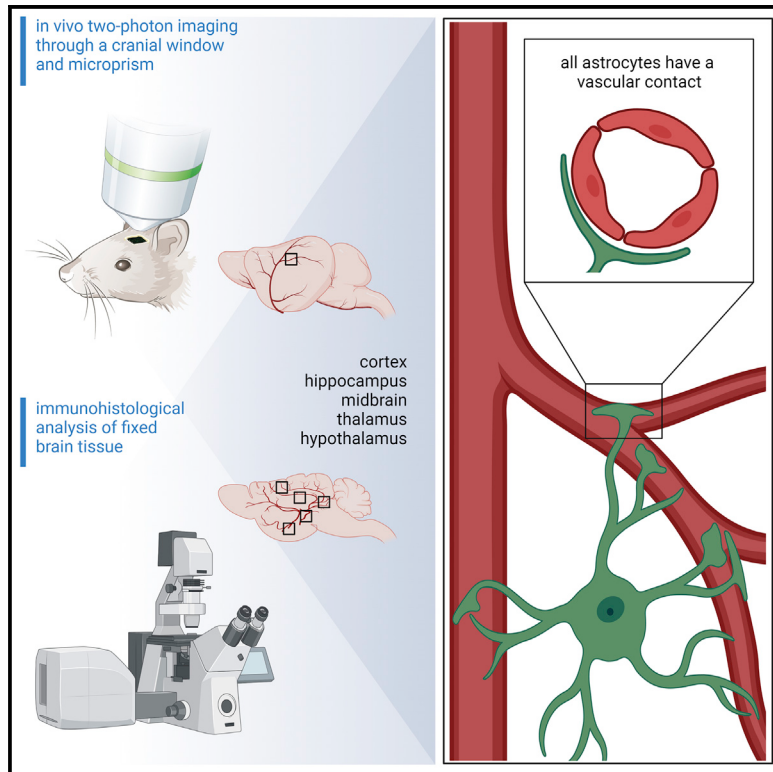


Direct vascular contact is a hallmark of cerebral astrocytes

Graphical abstract



Authors

Ladina Hösli, Marc Zuend, Gustav Bredell,
Henri S. Zanker,
Carlos Eduardo Porto de Oliveira,
Aiman S. Saab, Bruno Weber

Correspondence

bweber@pharma.uzh.ch

In brief

Using *in vivo* and *ex vivo* imaging, Hösli et al. find that all gray matter astrocytes in the investigated brain regions are connected to at least one vessel. Only in the hippocampus, which showed the lowest vessel density, did they discover single astrocytes without a direct vascular contact.

Highlights

- Of all gray matter astrocytes, 99.8% are connected to at least one blood vessel
- Most protoplasmic astrocytes maintain direct contact to three blood vessels
- Not astrocyte size, but vessel density, defines the number of contacted vessels
- Astrocytes without a direct vascular contact were found only in the hippocampus



Report

Direct vascular contact is a hallmark of cerebral astrocytes

Ladina Hösl^{1,2,4}, Marc Zuend^{1,2,4}, Gustav Bredell³, Henri S. Zanker^{1,2}, Carlos Eduardo Porto de Oliveira³, Aiman S. Saab^{1,2}, and Bruno Weber^{1,2,5,*}

¹University of Zurich, Institute of Pharmacology and Toxicology, 8057 Zurich, Switzerland

²Neuroscience Center Zurich, University and ETH Zurich, 8057 Zurich, Switzerland

³ETH Zurich, Computer Vision Laboratory, Department of Information Technology and Electrical Engineering, 8092 Zurich, Switzerland

⁴These authors contributed equally

⁵Lead contact

*Correspondence: bweber@pharma.uzh.ch

<https://doi.org/10.1016/j.celrep.2022.110599>

SUMMARY

Astrocytes establish extensive networks via gap junctions that allow each astrocyte to connect indirectly to the vasculature. However, the proportion of astrocytes directly associated with blood vessels is unknown. Here, we quantify structural contacts of cortical astrocytes with the vasculature *in vivo*. We show that all cortical astrocytes are connected to at least one blood vessel. Moreover, astrocytes contact more vessels in deeper cortical layers where vessel density is known to be higher. Further examination of different brain regions reveals that only the hippocampus, which has the lowest vessel density of all investigated brain regions, harbors single astrocytes with no apparent vascular connection. In summary, we show that almost all gray matter astrocytes have direct contact to the vasculature. In addition to the glial network, a direct vascular access may represent a complementary pathway for metabolite uptake and distribution.

INTRODUCTION

The precisely balanced microenvironment in the brain is maintained by an intact blood-brain barrier (BBB), separating the central nervous system (CNS) parenchyma from the systemic blood stream. While the BBB provides important protection against harmful substances and pathogens, it also facilitates the passage of vital molecules, such as energy substrates (Obermeier et al., 2013). As part of the neurovascular unit, astrocytes are thought to act as a connecting link between the metabolite suppliers (vessels) and the consumers (neurons), by regulating blood flow, metabolite availability, and neuronal activity. Protoplasmic astrocytes, located in the gray matter of the CNS, are among the structurally most complex cells in the brain. They are polarized cells that, on the one hand extend perivascular endfeet to closely contact the basal lamina of the vessel wall (Abbott et al., 2006), where they almost completely cover cerebral microvessels (Mathiisen et al., 2010). On the other hand, astrocytes engulf synapses with their processes, allowing them to sense neuronal activity (Araque et al., 1999; Santello et al., 2012), but also to modulate synaptic activity by neurotransmitter synthesis and removal, gliotransmission, and regulation of the local ionic environment (Araque et al., 2014; Bezzi and Volterra, 2001; Halassa et al., 2007a; Santello et al., 2019). Therefore, astrocytes are perfectly situated to locally regulate blood flow in an activity-dependent manner (Attwell et al., 2010; Gordon et al., 2008; Otsu et al., 2014). However, the exact pathways and extent to which astrocytes are involved in regulating vascular resistance remain an

active field of research. Importantly, astrocytes are highly interconnected via gap junction channels, forming large organized networks (Giaume and Liu, 2012; Hösl et al., 2022; Pannasch et al., 2011; Rouach et al., 2008; Theis et al., 2005). Astrocytic gap junction coupling allows for intercellular communication and distribution of ions, metabolites, and neurotransmitters (Giaume et al., 2010). The astrocytic network has also been described as playing a multi-faceted role in buffering extracellular potassium released during neuronal activity (Pannasch et al., 2011; Wallraff et al., 2006), and astrocytes are thought to integrate information of active neurons to locally increase cerebral blood flow via potassium signaling (Filosa et al., 2006). Interestingly, astrocytic networks have been spatially associated with neuronal functional units with high energy consumption, such as the barrels in the somatosensory cortex or the glomeruli of the olfactory bulb (Eilam et al., 2016; Houades et al., 2008; Roux et al., 2011). Capillaries, on the other hand, are evenly distributed and do not respect borders defined by functional units (Eilam et al., 2016; Hirsch et al., 2012; Keller et al., 2011; Shih et al., 2013; Tsai et al., 2009). This implies that astrocytes, rather than blood vessels, are responsible for the distribution of metabolites on the microscopic scale (Houades et al., 2008; Roux et al., 2011). Given the functional roles of astrocytes in neurovascular coupling and metabolic supply to neurons, a tight interaction of the astrocytic population with brain vasculature has to be expected (Zisis et al., 2021). However, the vast coupled network formed by astrocytes, that allows for a tailored distribution of blood-borne metabolites within the network, would make a



connection of every single astrocyte to the vasculature redundant. Nevertheless, the probability of an astrocyte-vessel connection in different brain regions is not known. In this study, we aimed to quantify the proportion of protoplasmic astrocytes directly associated with vasculature. By using sparse labeling strategies, we found that almost every individual astrocyte has a direct contact with a nearby blood vessel. Only in the hippocampus we found very few (~2.6%) astrocytes without an apparent connection to a blood vessel. The fact that every astrocyte is equipped with vascular endfeet, which allow for the uptake of blood-borne metabolites, questions the essentiality of astrocytic gap junction coupling for metabolite distribution.

RESULTS

Cortical astrocytes connect to at least one blood vessel

Astrocytic endfeet and the vessel wall are in close contact. However, previous studies investigating astrocyte-vessel interactions mainly focused on the degree of perivascular coverage by endfeet (El-Khoury et al., 2006; Kacem et al., 1998; Korogod et al., 2015; Mathiisen et al., 2010; Oberheim et al., 2009; Simard et al., 2003; Zisis et al., 2021). As a result, the fraction of astrocytes connected to the vasculature and the number of contacted vessels per astrocyte remained unknown. To acquire quantitative information about astrocyte-vessel interactions, we performed *in vivo* two-photon microscopy of sparsely labeled astrocytes in the somatosensory cortex (Figures 1A, S1A, and S1B). To identify vessels *in vivo*, we used a transgenic mouse line (Cldn5-GFP; Honkura et al., 2018) expressing GFP in endothelial cells controlled by the claudin 5 (Cldn5) promoter (Figures 1A, S1A, and S1B), or we used wild-type C57BL/6 mice that received a tail vein injection of Texas Red dextran (70 kDa) before imaging (Figures 1C and S1B). Sparse labeling of astrocytes was achieved using different adeno-associated virus (AAV)-delivery approaches (Figures S1A and S1B and see STAR Methods for more detail), leading to single astrocytes either expressing tdTomato (Figures 1A, S1A, and S1B) or GCaMP6s (Figures 1C and S1B). *In vivo* imaging of the somatosensory cortex was performed through a cranial window or through a microp prism to reach deeper cortical layers (Figures S1A and S1B). Astrocyte-vessel contacts were visually determined as an astrocytic endfoot, touching the vessel surface or wrapping around a blood vessel (see arrows in Figure 1A). A vessel was defined as the segment between two bifurcations (dashed lines in Figure 1C).

We analyzed a total of 697 individual astrocytes *in vivo* across all layers of the somatosensory cortex and found that each astrocyte contacted at least one blood vessel (Figure 1B and Table 1). The percentage distribution of the number of vessels contacted per astrocyte showed that most astrocytes contacted three blood vessels but as many as 9 vessels may be contacted by a single astrocyte (Figure 1B). Next, we wondered if the number of contacted vessels per individual astrocyte differed across cortical layers (Figures 1D and 1E). Indeed, we found that the number of contacted vessels per astrocyte had a bell-shaped distribution that peaked at layer 4 (L4; Figure 1D), with the majority of L4 astrocytes contacting five vessels (Figure 1E).

What could explain this layer-specific difference in vessel contacts per astrocyte? The probability of an astrocyte connecting

with nearby vessels is most likely determined by the vascular density as well as by the volume of the astrocyte. Vascular density varies significantly across cortical depths and cortical regions. Interestingly, in the somatosensory cortex, the lowest vascular density is observed in L1 and the highest vascular density in L4 (Blinder et al., 2013; Ji et al., 2021; Kirst et al., 2020; Schmid et al., 2019; Weber et al., 2008), which mirrors the high number of contacted vessels of investigated L4 astrocytes (Figures 1D and 1E). Moreover, astrocytic volume differences across cortical layers have been described earlier (Abdeladim et al., 2019; Halassa et al., 2007b; Lanjakornsiripan et al., 2018), reporting that L2/3 astrocytes in the somatosensory cortex occupy the largest territorial volume (Lanjakornsiripan et al., 2018). To investigate the volume of cortical astrocytes, we performed a Z-projection of the image stack to determine the size and shape of the astrocyte in the imaging (XY) and orthogonal planes (XZ and YZ). The size of each plane was then used to compute the minimum volume of the astrocyte (see STAR Methods for more detail). Indeed, when analyzing the volume of the investigated astrocytes, we observed that L2/3 astrocytes appeared to have the largest volumes, while L1 astrocytes were smallest in size (Figure 1F). In contrast to Lanjakornsiripan et al., 2018, we did not detect a significant difference between L2/3 and L4 astrocytes. Compared with confocal microscopy of optically cleared brain slices (Lanjakornsiripan et al., 2018), astrocytic volume measurements *in vivo* encounter the technical limitation of two-photon imaging, in which the spatial point spread function (PSF) may change with depth and thereby could distort volume measurements in deeper layers (Chaigneau et al., 2011; Helmchen and Denk, 2005). We sought to characterize the PSF of our two-photon microscope setup by mimicking a cranial window or a microp prism on a slide and imaging fluorescent beads through different depths of glycerol that has been reported to have a similar refractory index as brain tissue (Rosas et al., 2017; Sun et al., 2012; Figures S2A–S2F). Using this configuration, we found no depth-related alterations in the PSF (Figures S2C and S2F). However, we cannot completely rule out that changes in the PSF may impact astrocytic volume measurements in deeper layers. Surprisingly, even though L2/3 astrocytes seem to have the largest volumes, L4 astrocytes appeared to contact more vessels per astrocyte compared with astrocytes located in L2/3 (Figures 1D and 1E). Hence, apart from astrocytic volume, the high vessel density in L4 (Blinder et al., 2013; Ji et al., 2021; Kirst et al., 2020; Schmid et al., 2019; Weber et al., 2008) is likely an important factor that contributes to direct astrocyte-vessel interactions. More intriguingly, from 697 astrocytes, we did not find a single astrocyte without a contact to a blood vessel.

We analyzed a subset of the imaged astrocytes ($n = 106$) in more detail. In the three-dimensional (3D) visualization (Video S1 and Figure 2A), the tight interaction of an astrocyte with the surrounding vessels can be appreciated. In addition to the astrocyte volume and the number of contacted vessels per astrocyte reported previously, we calculated the astrocyte surface area and the contact area between an astrocyte and the associated vessels (Figures 2B–2F). As expected, the surface area of an astrocyte positively correlates with its volume (Figure 2B). Even though our data suggest that vessel density may correlate

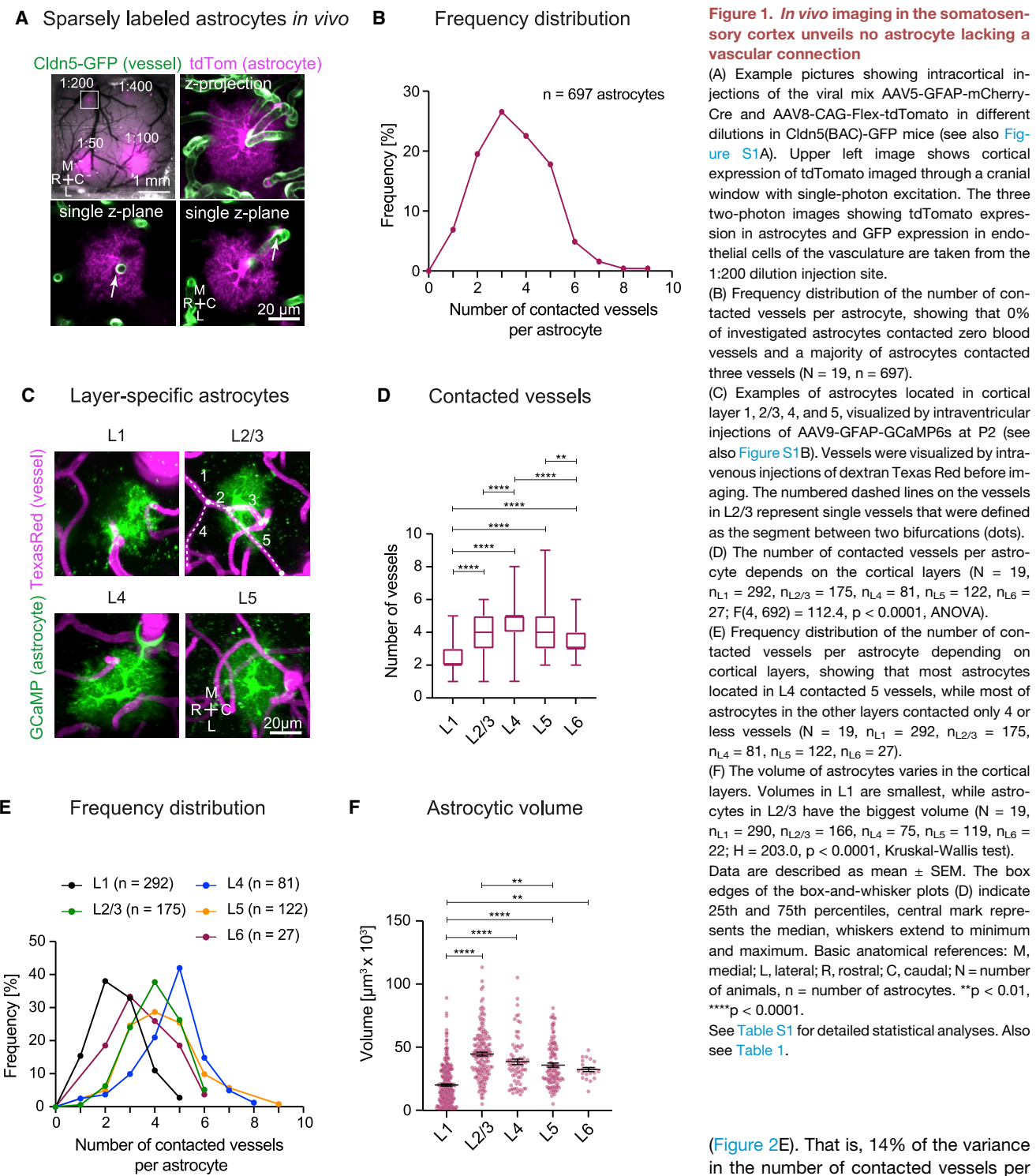


Figure 1. *In vivo* imaging in the somatosensory cortex unveils no astrocyte lacking a vascular connection

(A) Example pictures showing intracortical injections of the viral mix AAV5-GFAP-mCherry-Cre and AAV8-CAG-Flex-tdTomato in different dilutions in Cldn5(BAC)-GFP mice (see also Figure S1A). Upper left image shows cortical expression of tdTomato imaged through a cranial window with single-photon excitation. The three two-photon images showing tdTomato expression in astrocytes and GFP expression in endothelial cells of the vasculature are taken from the 1:200 dilution injection site.

(B) Frequency distribution of the number of contacted vessels per astrocyte, showing that 0% of investigated astrocytes contacted zero blood vessels and a majority of astrocytes contacted three vessels (N = 19, n = 697).

(C) Examples of astrocytes located in cortical layer 1, 2/3, 4, and 5, visualized by intraventricular injections of AAV9-GFAP-GCaMP6s at P2 (see also Figure S1B). Vessels were visualized by intravenous injections of dextran Texas Red before imaging. The numbered dashed lines on the vessels in L2/3 represent single vessels that were defined as the segment between two bifurcations (dots).

(D) The number of contacted vessels per astrocyte depends on the cortical layers (N = 19, n_{L1} = 292, n_{L2/3} = 175, n_{L4} = 81, n_{L5} = 122, n_{L6} = 27; F(4, 692) = 112.4, p < 0.0001, ANOVA).

(E) Frequency distribution of the number of contacted vessels per astrocyte depending on cortical layers, showing that most astrocytes located in L4 contacted 5 vessels, while most of astrocytes in the other layers contacted only 4 or less vessels (N = 19, n_{L1} = 292, n_{L2/3} = 175, n_{L4} = 81, n_{L5} = 122, n_{L6} = 27).

(F) The volume of astrocytes varies in the cortical layers. Volumes in L1 are smallest, while astrocytes in L2/3 have the biggest volume (N = 19, n_{L1} = 290, n_{L2/3} = 166, n_{L4} = 75, n_{L5} = 119, n_{L6} = 22; H = 203.0, p < 0.0001, Kruskal-Wallis test).

Data are described as mean ± SEM. The box edges of the box-and-whisker plots (D) indicate 25th and 75th percentiles, central mark represents the median, whiskers extend to minimum and maximum. Basic anatomical references: M: medial; L: lateral; R: rostral; C: caudal; N = number of animals, n = number of astrocytes. **p < 0.01, ***p < 0.0001.

See Table S1 for detailed statistical analyses. Also see Table 1.

more strongly with the number of contacted vessels per astrocyte than the astrocytic volume (Figure 1), there is also a positive correlation between the astrocytic volume and the number of contacted vessels. However, the fraction of the variance in the two variables that is “shared” (r^2) accounts only for 0.14

(Figure 2E). That is, 14% of the variance in the number of contacted vessels per astrocyte can be explained by the variation in astrocyte volume, and vice versa. Also, the bigger the astrocytic volume or the surface of an astrocyte the more contact area it has with the surrounding vessels (Figures 2C and 2D). Further, the more vessels an astrocyte contacts the bigger the total contact area with the vessels (Figure 2F).

Table 1. Astrocytes counted per cortical layer *in vivo*

Cortical layer	Astrocytes counted	Astrocytes without a connection	Number of connections (mean ± SEM)
L1	292	0	2.5 ± 0.07
L2/3	175	0	4.0 ± 0.08
L4	81	0	4.7 ± 0.15
L5	122	0	4.3 ± 0.12
L6	27	0	3.6 ± 0.22
Total	697	0	3.5 ± 0.05

The vast majority of gray matter astrocytes in the brain is connected to a blood vessel

Next, we wondered if astrocytes located in other brain areas have a direct contact to blood vessels as well. To address this question, we used an inducible, transgenic approach to achieve widespread sparse labeling of astrocytes throughout the brain (Figure 3). We crossed the *Aldh1l1-Cre/ERT2* transgenic line (Srinivasan et al., 2016) with the Cre-dependent GCaMP6s reporter line Ai96 (Madisen et al., 2015) and injected their double transgenic offspring with a single dose of tamoxifen (Figure 3A) in order to achieve sparse labeling of astrocytes (Figure 3B). Using confocal microscopy on sagittal brain sections, we examined the morphological interaction of astrocytes and vessels in cortex, hippocampus, midbrain, thalamus, and hypothalamus (Figures 3B and 3C). In total, we analyzed 1,114 single astrocytes from three animals and found that a majority of astrocytes in all brain regions had contacts with three vessels (Figures 3E and 3F and Table 2), with a similar distribution of the number of vessels contacted per astrocyte as observed in the somatosensory cortex *in vivo* (Figure 1B). Only in the hippocampus, we found three astrocytes that had no clear connection with a blood vessel (asterisk in Figure 3Di-iii) that accounted only for 2.6% of all hippocampal astrocytes examined (Figure 3F). Given that astrocytes in all investigated brain regions contacted at least one blood vessel (Figure 3F), except the hippocampal astrocytes, we wondered if the latter may correlate with differences in the astrocytic size or vascular density in the hippocampus. Fitting an ellipse to the segmented astrocytes allowed us to calculate the major diagonal, $D_1 = 62.7 \pm 0.4$, and minor diagonal, $D_2 = 57.3 \pm 0.4 \mu\text{m}$ (mean ± SEM of all astrocytes; Figures S3A and S3B), as well as the area, $A = 1,565 \pm 19.34 \mu\text{m}^2$ (mean ± SEM of all astrocytes, Figure 3G), of each astrocyte. There was no difference of hippocampal astrocytes compared with astrocytes located in the other brain regions (Figures 3G, S3A, and S3B), suggesting that astrocyte gross morphology is not the key determinant for the number of contacted vessels per astrocytes. As already seen in the *in vivo* data from the somatosensory cortex (Figures 1D and 1E), vessel density may be more critical. Published data revealed that the mean minimal distance of any given point in the brain tissue to the closest blood vessel measures 10–30 μm (Risser et al., 2009; Sakadžić et al., 2014; Shaw et al., 2021). Therefore, considering the measured diameters of astrocytes and the known spatial distribution of the vasculature, astrocytes cannot fit between two vessels without forming a contact point to at least one vessel. However, vessel

density is known to vary between different brain regions (Bohn et al., 2016; Ji et al., 2021; Kirst et al., 2020; Shaw et al., 2021; Todorov et al., 2020; Zhang et al., 2019). Indeed, we found that the hippocampus had the lowest vessel density compared with the other brain regions examined (Figure 1H). Hence, the lower vessel density correlates with the rare observation of astrocytes without a direct contact to a vessel in the hippocampus (Figures 2E and 2H). These measurements are in line with recently published data showing that vascular density in the hippocampus is lower compared with other gray matter regions (Bohn et al., 2016; Ji et al., 2021; Kirst et al., 2020; Shaw et al., 2021; Todorov et al., 2020; Zhang et al., 2019). Together, the two sets of data show that most protoplasmic astrocytes (1,808 out of a total of 1,811 astrocytes investigated in the somatosensory cortex *in vivo* and in various brain regions in histological sections; 99.83%) maintain a direct contact to the vasculature. Also, the intensity of astrocyte-vessel interaction may be determined by vascular density, rather than the size of an astrocyte.

DISCUSSION

In the current study, we used sparse labeling of astrocytes to study astrocyte-vessel interactions in different gray matter regions *in vivo* and in histological sections. We found that all 697 investigated astrocytes in the somatosensory cortex *in vivo* were connected to at least one vessel and that the number of associated vessels per astrocyte correlated with the known varying vessel density across the cortical layers (Blinder et al., 2013; Ji et al., 2021; Kirst et al., 2020; Schmid et al., 2019; Weber et al., 2008). Also, we investigated a total of 1,114 astrocytes in the cortex, hippocampus, midbrain, thalamus, and hypothalamus in histological sections and found only three astrocytes without a vascular connection—all three astrocytes were located in the hippocampus, where vascular density was lowest compared with the other examined brain regions.

Out of all investigated astrocytes *in vivo* and in histological sections, only three hippocampal astrocytes revealed no direct interaction with a blood vessel (0.17%). Given that astrocytes form extensive intercellular networks that have been suggested as playing a key role in metabolite distribution (Cooper et al., 2020; Giaume et al., 2010), we were surprised to find so few astrocytes without direct access to the vasculature. Indeed, the metabolic support function of the astrocytic network involving lactate supply to neurons was described in different brain regions regulating various cognitive behaviors (Clasadonte et al., 2017; Murphy-Royal et al., 2020; Rouach et al., 2008). The results of the present study raise the question why gap junction coupling of astrocytes is required for metabolic support of neurons when almost all astrocytes have access to blood vessels—the metabolic source. Interestingly, many important biological systems display a robustness against perturbations, which can be ascribed to functionally redundant pathways (Hartman et al., 2001). This includes redundant genes compensating for loss of gene function (Wagner, 2005), the circle of Willis generating redundant connections ensuring brain perfusion (Alpers et al., 1959), as

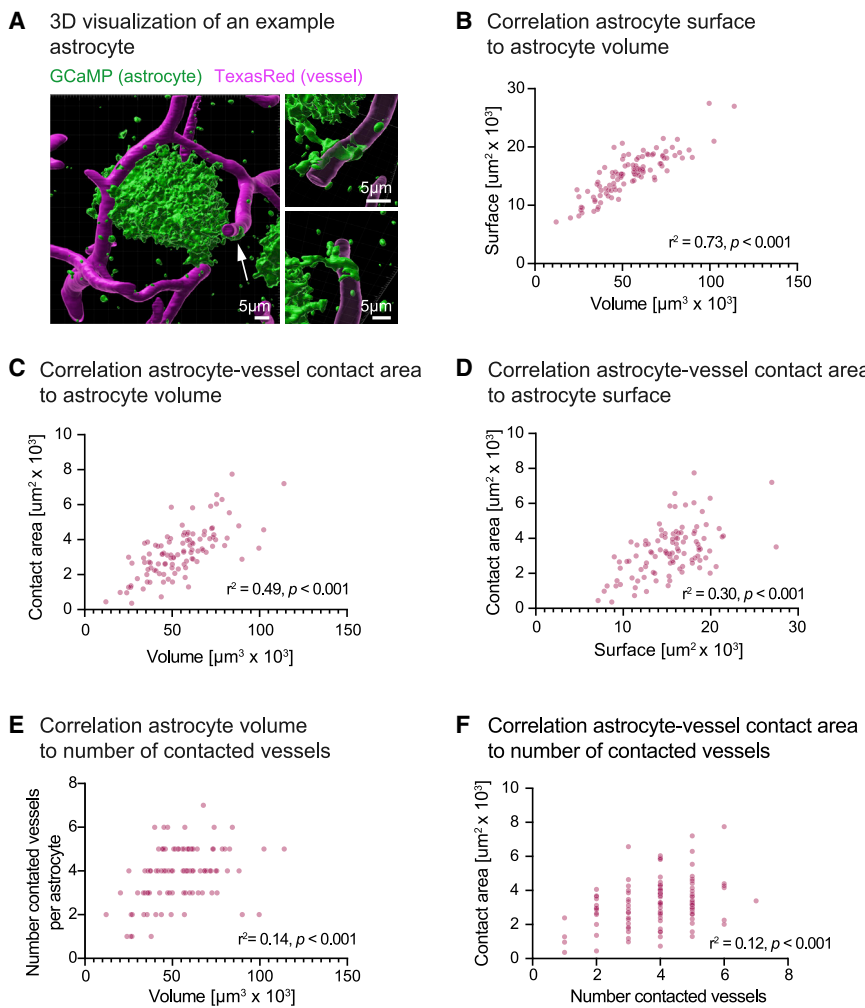


Figure 2. Calculations of astrocyte surface and volume, astrocyte-vessel contact area, and number of contacted vessels per astrocyte for a subset of astrocytes and their correlation analyses

(A) A 3D reconstruction of an L2/3 astrocyte (green) and the surrounding vessels (magenta; also see [Video S1](#) for 3D animation). White arrow highlights an astrocytic endfoot ensheathing a cortical vessel (left). Enhanced visualization of the highlighted endfoot (white arrow) from the top (upper) and bottom (lower). To evaluate the nature of the contact, the opacity was adjusted to transparency 0 (right).

(B) Comparison of the astrocyte surface versus astrocyte volume ($N = 4, n = 106$).

(C) Comparison of the astrocyte-vessel contact area versus astrocyte volume ($N = 4, n = 106$).

(D) Comparison of the astrocyte-vessel contact area versus astrocyte surface ($N = 4, n = 106$).

(E) Comparison of the number of contacted vessels per astrocyte versus astrocyte volume ($N = 4, n = 106$).

(F) Comparison of the astrocyte-vessel contact area versus the number of contacted vessels per astrocyte ($N = 4, n = 106$).

See [Table S1](#) for detailed statistical analyses. N = number of animals, n = number of astrocytes.

stressed tissue while at the same time increasing the burden for the healthy tissue.

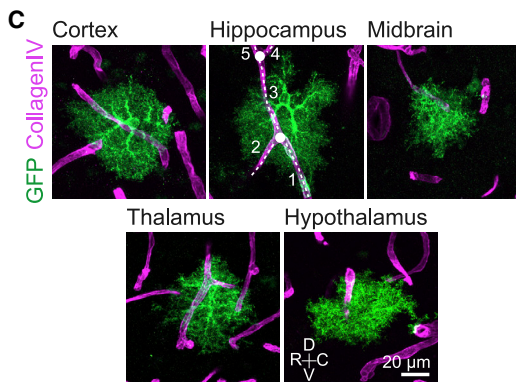
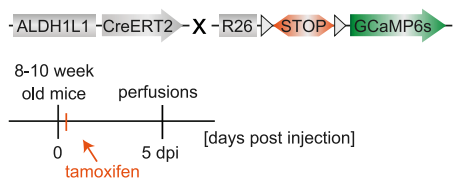
Limitations of the study

The combination of *in vivo* and fixed tissue imaging was chosen to overcome potential artifacts based on tissue alterations caused by fixation protocols ([Korogod et al., 2015](#)). We

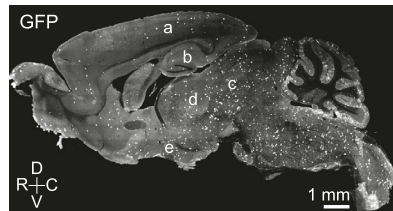
well as metabolic pathways ensuring proper cellular function ([Behre et al., 2008](#)). In the brain, appropriate distribution of metabolites to neuronal compartments is vital for neuronal function ([Magnotti et al., 2011](#); [Menichella et al., 2003](#); [Odermann et al., 2003](#)). Therefore, it is possible that redundant pathways for efficient metabolite distribution exist in the brain. Direct astrocytic contact to the vasculature and an indirect vascular connection via gap junction coupling may be an example of such redundancy. Interestingly, redundant pathways may also display distinct functional roles under certain conditions ([Harrison et al., 2007](#); [Sambamoorthy and Raman, 2018](#)). Direct and indirect vascular contact may substitute for each other during basal brain activity. Possibly, both pathways are required for complex cognitive functions, such as learning and memory. It is also conceivable that one of the pathways may take over when astrocytic coupling is perturbed ([Hösl et al., 2022](#)) or during pathological conditions ([Cooper et al., 2020](#)). Indeed, it has been shown that astrocytic gap junction coupling is important for the redistribution of (glycogen-derived) metabolites from healthy tissue to stressed tissue ([Cooper et al., 2020](#)), thereby minimizing the damage of the

used sparse labeling to investigate single astrocyte morphology and the interaction with the vasculature. Therefore, the labeling method potentially creates a bias and had to be validated with caution. We pursued several strategies ([Figures 1, S1, and 3](#)) to ensure targeting the majority of astrocyte populations ([Chai et al., 2017](#); [Khakh and Deneen, 2019](#); [Lanjakornsiripan et al., 2018](#); [Lin et al., 2017](#); [Morel et al., 2017](#)). The strategies included (1) the use of different AAV serotypes (a mix of AAV5-GFP-mCherry-Cre + AAV8-CAG-flex-tdTOMO, and AAV9-GFP-GCaMP6s only; [Figure S1](#)) to minimize cellular selectivity of AAVs; (2) different routes and timings of AAV administration (intraventricular injections in pups and intracortical injections in adult mice; [Figure S1](#)) to reduce the effect on tropism and biodistribution of the transgene expression ([Chakrabarty et al., 2013](#)); (3) different labeling approaches (AAV-mediated transgene expression and transgene induction with tamoxifen) to rule out a bias toward labeling of juxtaglomerular astrocytes, because tamoxifen likely reaches the brain via the bloodstream; and (4) the use of two widely expressed promoters (ALDH1L1 and GFAP; [Pannasch et al., 2011](#); [Srinivasan et al., 2016](#)).

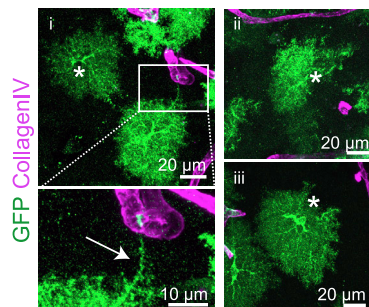
A Mouse model and sparse labeling protocol



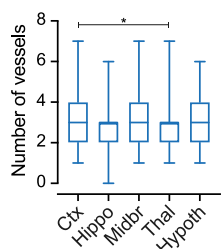
B Sparse labeling of cerebral astrocytes



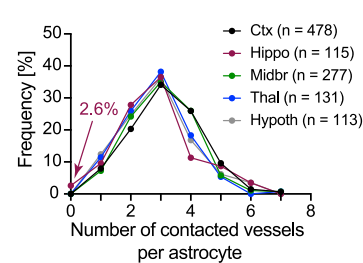
D Hippocampal astrocytes without vessel contact



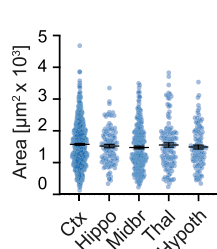
E Contacted vessels



F Frequency distribution



G Astrocyte size



H Vessel density

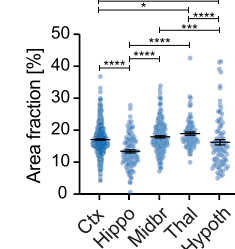


Figure 3. Almost all gray matter astrocytes are connected to at least one blood vessel

(A) Generation of ALDH1L1^{CreERT2/+}: ROSA26-floxed-STOP-GCaMP6s (Ai96) reporter mice. Tamoxifen was injected once in adult mice and analysis was performed at 5 days post-injection (dpi).

(B) Overview image of a sagittal brain section showing sparsely labeled astrocytes in all analyzed brain areas: a. cortex; b. hippocampus; c. midbrain; d. thalamus; and e. hypothalamus.

(C) Confocal maximum intensity projections showing examples of sparsely labeled astrocytes (anti-GFP antibody, green) and stained vessels (anti-collagen IV antibody, magenta) for each brain region of interest. One vessel (dashed lines in hippocampus example) is defined as the part of the vasculature between two bifurcations (dots).

(D) The three hippocampal astrocytes we found without obvious connection to the vasculature are marked with an asterisk (i-iii). The magnification of (i) shows that astrocytes can extend very long and delicate processes to far away vessels.

(E) Number of connected vessels per astrocyte in the investigated brain regions. Except for the three hippocampal astrocytes shown in (D), every investigated astrocyte showed a connection to at least one vessel ($N = 3$, $n_{\text{ctx}} = 478$, $n_{\text{hippo}} = 115$, $n_{\text{midbr}} = 277$, $n_{\text{thal}} = 131$, $n_{\text{hypoth}} = 113$; $F(4, 1109) = 3.5$, $p = 0.0077$, ANOVA).

(F) Frequency distribution of number of contacted vessels per astrocyte in the investigated gray matter regions. Note that only in the hippocampus 2.6% of astrocytes lacked a connection to vasculature ($N = 3$, $n_{\text{ctx}} = 478$, $n_{\text{hippo}} = 115$, $n_{\text{midbr}} = 277$, $n_{\text{thal}} = 131$, $n_{\text{hypoth}} = 113$).

(G) Astrocytic area in the different brain regions of interest are similar ($N = 3$, $n_{\text{ctx}} = 644$, $n_{\text{hippo}} = 114$, $n_{\text{midbr}} = 276$, $n_{\text{thal}} = 131$, $n_{\text{hypoth}} = 113$; $H = 4.848$, $p = 0.3033$, Kruskal-Wallis test).

(H) Vessel density varied in the investigated brain regions ($N = 3$, $n_{\text{ctx}} = 488$, $n_{\text{hippo}} = 114$, $n_{\text{midbr}} = 179$, $n_{\text{thal}} = 88$, $n_{\text{hypoth}} = 91$; $H = 83.82$, $p < 0.0001$, Kruskal-Wallis test).

Data are described as mean \pm SEM. The box edges of the box-and-whisker plot (E) indicate 25th and 75th percentiles; central mark represents the median. Whiskers extend to minimum and maximum. Basic anatomical references: D, dorsal; V, ventral; R, rostral; C, caudal. N = number of animals, n = number of astrocytes.

See Table S1 for detailed statistical analyses. See also Table 2.

Nevertheless, subtype selectivity cannot be excluded with certainty. Along the same lines, we cannot entirely exclude that different astrocyte populations were labeled

using the respective strategies mentioned above. Nevertheless, all strategies converged with respect to the main result.

Table 2. Astrocytes counted per brain region in histological sections

Brain region	Astrocytes counted	Astrocytes without a connection	Number of connections mean \pm SEM
Cortex	478	0	3.2 \pm 0.05
Hippocampus	115	3	2.8 \pm 0.12
Midbrain	277	0	3.1 \pm 0.07
Thalamus	131	0	2.8 \pm 0.1
Hypothalamus	113	0	2.9 \pm 0.11
Total	1,114	3	3.0 \pm 0.04

Because this study is based solely on morphology, no conclusions about the functionality of the astrocyte-vessel interactions can be drawn at this point. Future studies should focus on different contact types, such as center versus periphery of the astrocyte or different vessel types. Furthermore, a correlative imaging study combining electron and fluorescence microscopy will be needed to elucidate whether the definition of vascular contact chosen here based on mere proximity is sufficient.

In summary, we found that most of the cerebral astrocytes are connected to at least one blood vessel. It is conceivable that this direct vascular contact complements astrocytic gap junctional coupling to ensure metabolite distribution in the brain, which is essential for neural survival. This may also explain the absence of neurodegeneration when astrocytes were decoupled in adult mice (Hösli et al., 2022). We also observed that region-specific differences in vessel density correlate well with the number of contacts astrocytes have with the vasculature. The role of astrocytic gap junction coupling in metabolic support may thus be more critical in brain regions with lower vessel densities such as the hippocampus. This functional relationship of vessel density, number of vessels connected to individual astrocytes and astrocytic coupling, needs to be resolved in future studies.

STAR★METHODS

Detailed methods are provided in the online version of this paper and include the following:

- KEY RESOURCES TABLE
- RESOURCE AVAILABILITY

- Lead contact
- Materials availability
- Data and code accessibility

- EXPERIMENTAL MODEL AND SUBJECT DETAILS

- METHOD DETAILS

- Tamoxifen treatment
- Intraventricular viral injections in pups
- Cranial window and intracortical viral injections
- Micropism implantation
- Fluorescence check
- Visualization of blood plasma during imaging
- Microscope design and *in vivo* imaging parameters
- Pixel size calibration

- PSF measurements and deconvolution
- Immunohistology
- Image acquisition of histological preparations
- Astrocyte size analysis and astrocyte properties
- Correlation analysis and 3D visualization
- Vessel density of immunohistological section

- QUANTIFICATION AND STATISTICAL ANALYSIS

SUPPLEMENTAL INFORMATION

Supplemental information can be found online at <https://doi.org/10.1016/j.celrep.2022.110599>.

ACKNOWLEDGMENTS

We thank all lab members of the Weber and Saab group for support and frequent discussions. We would also like to thank Jean-Charles Paterna and the Viral Vector Facility of the Neuroscience Center Zurich (ZNZ) for viral productions and the Center for Microscopy and Image Analysis (ZMB) for the software resources. We thank Noemi Binini and Zoe Looser for genotyping help. Graphical abstract was created with BioRender. B.W. is supported by the Swiss National Science Foundation (3100030_182703). A.S.S. received support from the Cloëtta Foundation and from the Swiss National Science Foundation (Eccellenza 187000).

AUTHOR CONTRIBUTIONS

Conceptualization, L.H., M.Z., A.S.S., and B.W.; methodology, L.H. and M.Z.; software, M.Z., G.B., and C.E.P.d.O.; formal analysis, L.H., M.Z., G.B., and C.E.P.d.O.; investigations, M.Z., L.H., and H.S.Z.; writing – original draft, L.H., M.Z., and A.S.S.; visualization, L.H. and M.Z.; writing – review & editing, L.H., M.Z., G.B., H.S.Z., C.E.P.d.O., A.S.S., and B.W.; funding acquisition, B.W. All authors discussed the results and contributed to revision of the manuscript.

DECLARATION OF INTERESTS

The authors declare no competing financial interests.

Received: September 7, 2021

Revised: February 9, 2022

Accepted: March 9, 2022

Published: April 5, 2022

REFERENCES

- Abbott, N.J., Rönnbäck, L., and Hansson, E. (2006). Astrocyte–endothelial interactions at the blood–brain barrier. *Nat. Rev. Neurosci.* 7, 41–53.
- Abdeladim, L., Matho, K.S., Clavreul, S., Mahou, P., Sintes, J.M., Solinas, X., Arganda-Carreras, I., Turney, S.G., Lichtman, J.W., Chessel, A., et al. (2019). Multicolor multiscale brain imaging with chromatic multiphoton serial microscopy. *Nat. Commun.* 10, 1–14.
- Alpers, B.J., Berry, R.G., and Paddison, R.M. (1959). Anatomical studies of the circle of Willis in normal brain. *Arch. Neurol. Psychiatr.* 81, 409.
- Araque, A., Parpura, V., Sanzgiri, R.P., and Haydon, P.G. (1999). Tripartite synapses: glia, the unacknowledged partner. *Trends Neurosci.* 22, 208–215.
- Araque, A., Carmignoto, G., Haydon, P.G., Oliet, S.H.R., Robitaille, R., and Volterra, A. (2014). Gliotransmitters travel in time and space. *Neuron* 81, 728–739.
- Attwell, D., Buchan, A.M., Charpak, S., Lauritzen, M., Macvicar, B.A., and Newman, E.A. (2010). Glial and neuronal control of brain blood flow. *Nature* 468, 232–243.
- Behre, J., Wilhelm, T., von Kamp, A., Ruppin, E., and Schuster, S. (2008). Structural robustness of metabolic networks with respect to multiple knock-outs. *J. Theor. Biol.* 252, 433–441.

- Bezzi, P., and Volterra, A. (2001). A neuron–glia signalling network in the active brain. *Curr. Opin. Neurobiol.* 11, 387–394.
- Blinder, P., Tsai, P.S., Kauhfeld, J.P., Knutson, P.M., Suhl, H., and Kleinfeld, D. (2013). The cortical angiome: an interconnected vascular network with noncolumnar patterns of blood flow. *Nat. Neurosci.* 16, 889–897.
- Bohn, K.A., Adkins, C.E., Mittapalli, R.K., Terrell-Hall, T.B., Mohammad, A.S., Shah, N., Dolan, E.L., Nounou, M.I., and Lockman, P.R. (2016). Semi-automated rapid quantification of brain vessel density utilizing fluorescent microscopy. *J. Neurosci. Methods* 270, 124–131.
- Chai, H., Diaz-Castro, B., Shigetomi, E., Monte, E., Octeau, J.C., Yu, X., Cohn, W., Rajendran, P.S., Vondriska, T.M., Whitelegge, J.P., et al. (2017). Neural circuit-specialized astrocytes: transcriptomic, proteomic, morphological, and functional evidence. *Neuron* 95, 531–549.e9.
- Chaigneau, E., Wright, A.J., Poland, S.P., Girkin, J.M., and Silver, R.A. (2011). Impact of wavefront distortion and scattering on 2-photon microscopy in mammalian brain tissue. *Opt. Express* 19, 22755.
- Chakrabarty, P., Rosario, A., Cruz, P., Sieminski, Z., Ceballos-Diaz, C., Crosby, K., Jansen, K., Borchelt, D.R., Kim, J.Y., Jankowsky, J.L., et al. (2013). Capsid serotype and timing of injection determines AAV transduction in the neonatal mice brain. *PLoS One* 8, 0–8.
- Clasadonte, J., Scemes, E., Wang, Z., Boison, D., and Haydon, P.G. (2017). Connexin 43-mediated astroglial metabolic networks contribute to the regulation of the sleep-wake cycle. *Neuron* 95, 1365–1380.e5.
- Cooper, M.L., Pasini, S., Lambert, W.S., D'Alessandro, K.B., Yao, V., Risner, M.L., and Calkins, D.J. (2020). Redistribution of metabolic resources through astrocyte networks mitigates neurodegenerative stress. *Proc. Natl. Acad. Sci. U S A* 117, 18810–18821.
- Elbam, R., Aharoni, R., Arnon, R., and Malach, R. (2016). Astrocyte morphology is confined by cortical functional boundaries in mammals ranging from mice to human. *Elife* 5, 1–18.
- El-Khoury, N., Braun, A., Hu, F., Pandey, M., Nedergaard, M., Lagamma, E.F., and Ballabh, P. (2006). Astrocyte end-feet in germinal matrix, cerebral cortex, and white matter in developing infants. *Pediatr. Res.* 59, 673–679.
- Filosa, J.A., Bonev, A.D., Straub, S.V., Meredith, A.L., Wilkerson, M.K., Aldrich, R.W., and Nelson, M.T. (2006). Local potassium signaling couples neuronal activity to vasodilation in the brain. *Nat. Neurosci.* 9, 1397–1403.
- Giaume, C., and Liu, X. (2012). From a glial syncytium to a more restricted and specific glial networking. *J. Physiol.* 106, 34–39.
- Giaume, C., Koulakoff, A., Roux, L., Holcman, D., and Rouach, N. (2010). Astroglial networks: a step further in neuroglial and gliovascular interactions. *Nat. Rev. Neurosci.* 11, 87–99.
- Girish, V., and Vijayalakshmi, A. (2004). Affordable image analysis using NIH Image/ImageJ. *Indian J. Cancer* 41, 47.
- Gordon, G.R.J., Choi, H.B., Rungta, R.L., Ellis-Davies, G.C.R., and MacVicar, B.A. (2008). Brain metabolism dictates the polarity of astrocyte control over arterioles. *Nature* 456, 745–749.
- Halassa, M.M., Fellin, T., and Haydon, P.G. (2007a). The tripartite synapse: roles for gliotransmission in health and disease. *Trends Mol. Med.* 13, 54–63.
- Halassa, M.M., Fellin, T., Takano, H., Dong, J.-H., and Haydon, P.G. (2007b). Synaptic islands defined by the territory of a single astrocyte. *J. Neurosci.* 27, 6473–6477.
- Harrison, R., Papp, B., Pál, C., Oliver, S.G., and Delneri, D. (2007). Plasticity of genetic interactions in metabolic networks of yeast. *Proc. Natl. Acad. Sci. U S A* 104, 2307–2312.
- Hartman, J.L., Garvik, B., and Hartwell, L. (2001). Cell Biology: principles for the buffering of genetic variation. *Science* 291, 1001–1004.
- Helmlchen, F., and Denk, W. (2005). Deep tissue two-photon microscopy. *Nat. Methods* 2, 932–940.
- Hirsch, S., Reichold, J., Schneider, M., Székely, G., and Weber, B. (2012). Topology and hemodynamics of the cortical cerebrovascular system. *J. Cereb. Blood Flow Metab.* 32, 952–967.
- Honkura, N., Richards, M., Laviña, B., Sáinz-Jaspeado, M., Betsholtz, C., and Claesson-Welsh, L. (2018). Intravital imaging-based analysis tools for vessel identification and assessment of concurrent dynamic vascular events. *Nat. Commun.* 9, 2746.
- Hösl, L., Binini, N., Ferrari, K.D., Thieren, L., Looser, Z.J., Zuend, M., Zanker, H.S., Berry, S., Holub, M., Möbius, W., et al. (2022). Decoupling astrocytes in adult mice impairs synaptic plasticity and spatial learning. *Cell Reports* 38 (10). <https://doi.org/10.1016/j.celrep.2022.110484>.
- Houades, V., Koulakoff, A., Ezan, P., Seif, I., and Giaume, C. (2008). Gap junction-mediated astrocytic networks in the mouse barrel cortex. *J. Neurosci.* 28, 5207–5217.
- Ji, X., Ferreira, T., Friedman, B., Liu, R., Liechty, H., Bas, E., Chandrashekhar, J., and Kleinfeld, D. (2021). Brain microvasculature has a common topology with local differences in geometry that match metabolic load. *Neuron* 109, 1168–1187.e13.
- Kacem, K., Lacombe, P., Seylaz, J., and Bonvento, G. (1998). Structural organization of the perivascular astrocyte endfeet and their relationship with the endothelial glucose transporter: a confocal microscopy study. *Glia* 23, 1–10.
- Keller, A.L., Schüz, A., Logothetis, N.K., and Weber, B. (2011). Vascularization of cytochrome oxidase-rich blobs in the primary visual cortex of squirrel and macaque monkeys. *J. Neurosci.* 31, 1246–1253.
- Khakh, B.S., and Deneen, B. (2019). The emerging nature of astrocyte diversity. *Annu. Rev. Neurosci.* 42, 187–207.
- Kim, J.-Y., Ash, R.T., Ceballos-Diaz, C., Levites, Y., Golde, T.E., Smirnakis, S.M., and Jankowsky, J.L. (2013). Viral transduction of the neonatal brain delivers controllable genetic mosaicism for visualising and manipulating neuronal circuits *in vivo*. *Eur. J. Neurosci.* 37, 1203–1220.
- Kirst, C., Skriabine, S., Vieites-Prado, A., Topilko, T., Bertin, P., Gerschenfeld, G., Verny, F., Topilko, P., Michalski, N., Tessier-Lavigne, M., et al. (2020). Mapping the fine-scale organization and plasticity of the brain vasculature. *Cell* 180, 780–795.e25.
- Korogod, N., Petersen, C.C.H., and Knott, G.W. (2015). Ultrastructural analysis of adult mouse neocortex comparing aldehyde perfusion with cryo fixation. *Elife* 4, 1–17.
- Laanjakonsiripan, D., Pior, B.J., Kawaguchi, D., Furutachi, S., Tahara, T., Katayama, Y., Suzuki, Y., Fukazawa, Y., and Gotoh, Y. (2018). Layer-specific morphological and molecular differences in neocortical astrocytes and their dependence on neuronal layers. *Nat. Commun.* 9, 1623.
- Lee, T.C., Kashyap, R.L., and Chu, C.N. (1994). Building skeleton models via 3-D medial surface Axis thinning algorithms. *CVGIP Graph. Models Image Process.* 56, 462–478.
- Li, C.H., and Lee, C.K. (1993). Minimum cross entropy thresholding. *Pattern Recogn.* 26, 617–625.
- Lin, C.-C.J., Yu, K., Hatcher, A., Huang, T.-W., Lee, H.K., Carlson, J., Weston, M.C., Chen, F., Zhang, Y., Zhu, W., et al. (2017). Identification of diverse astrocyte populations and their malignant analogs. *Nat. Neurosci.* 20, 396–405.
- Madisen, L., Garner, A.R., Shimaoka, D., Chuong, A.S., Klapoetke, N.C., Li, L., van der Bourg, A., Niino, Y., Egolf, L., Monetti, C., et al. (2015). Transgenic mice for intersectional targeting of neural sensors and effectors with high specificity and performance. *Neuron* 85, 942–958.
- Magnotti, L.M., Goodenough, D.A., and Paul, D.L. (2011). Deletion of oligodendrocyte Cx32 and astrocyte Cx43 causes white matter vacuolation, astrocyte loss and early mortality. *Glia* 59, 1064–1074.
- Mathiisen, T.M., Lehre, K.P., Danbolt, N.C., and Ottersen, O.P. (2010). The perivascular astroglial sheath provides a complete covering of the brain microvessels: an electron microscopic 3D reconstruction. *Glia* 58, 1094–1103.
- Mayrhofer, J.M., Haiss, F., Haenni, D., Weber, S., Zuend, M., Barrett, M.J.P., Ferrari, K.D., Maechler, P., Saab, A.S., Stobart, J.L., et al. (2015). Design and performance of an ultra-flexible two-photon microscope for *in vivo* research. *Biomed. Opt. Express* 6, 4228.
- Menichella, D.M., Goodenough, D.A., Sirkowski, E., Scherer, S.S., and Paul, D.L. (2003). Connexins are critical for normal myelination in the CNS. *J. Neurosci.* 23, 5963–5973.

- Morel, L., Chiang, M.S.R., Higashimori, H., Shoneye, T., Iyer, L.K., Yelick, J., Tai, A., and Yang, Y. (2017). Molecular and functional properties of regional astrocytes in the adult brain. *J. Neurosci.* 37, 3956–4016.
- Murphy-Royal, C., Johnston, A.D., Boyce, A.K.J., Diaz-Castro, B., Institoris, A., Peringod, G., Zhang, O., Stout, R.F., Spray, D.C., Thompson, R.J., et al. (2020). Stress gates an astrocytic energy reservoir to impair synaptic plasticity. *Nat. Commun.* 11, 2014.
- Oberheim, N.a., Takano, T., Han, X., He, W., Lin, J.H.C., Wang, F., Xu, Q., Wyatt, J.D., Pilcher, W., Ojemann, J.G., et al. (2009). Uniquely hominid features of adult human astrocytes. *J. Neurosci.* 29, 3276–3287.
- Obermeier, B., Daneman, R., and Ransohoff, R.M. (2013). Development, maintenance and disruption of the blood-brain barrier. *Nat. Med.* 19, 1584–1596.
- Odermatt, B., Wellershaus, K., Wallraff, A., Seifert, G., Degen, J., Euwens, C., Fuss, B., Büsow, H., Schilling, K., Steinhäuser, C., et al. (2003). Connexin 47 (Cx47)-Deficient mice with enhanced green fluorescent protein reporter gene reveal predominant oligodendrocytic expression of Cx47 and display vacuolized myelin in the CNS. *J. Neurosci.* 23, 4549–4559.
- Otsu, Y., Couchman, K., Lyons, D.G., Collot, M., Agarwal, A., Mallet, J.-M., Pfrieger, F.W., Bergles, D.E., and Charpak, S. (2014). Calcium dynamics in astrocyte processes during neurovascular coupling. *Nat. Neurosci.* 18, 210–218.
- Pannasch, U., Vargova, L., Reingruber, J., Ezan, P., Holcman, D., Giaume, C., Sykova, E., and Rouach, N. (2011). Astroglial networks scale synaptic activity and plasticity. *Proc. Natl. Acad. Sci. U S A* 108, 8467–8472.
- Pologruto, T.A., Sabatini, B.L., and Svoboda, K. (2003). ScanImage: flexible software for operating laser scanning microscopes. *Biomed. Eng. Online* 2, 13.
- Risser, L., Plouraboué, F., Cloetens, P., and Fonta, C. (2009). A 3D-investigation shows that angiogenesis in primate cerebral cortex mainly occurs at capillary level. *Int. J. Dev. Neurosci.* 27, 185–196.
- Rosas, I.P., Contreras, J.L., Salmones, J., Tapia, C., Zeifert, B., Navarrete, J., Vázquez, T., and García, D.C. (2017). Catalytic dehydration of glycerol to acrolein over a catalyst of Pd/LaY zeolite and comparison with the chemical equilibrium. *Catalysts* 7, 1–29.
- Rouach, N., Koulakoff, A., Abudara, V., Willecke, K., and Giaume, C. (2008). Astroglial metabolic networks sustain hippocampal synaptic transmission. *Science* 322, 1551–1555.
- Roux, L., Benchenane, K., Rothstein, J.D., Bonvento, G., and Giaume, C. (2011). Plasticity of astroglial networks in olfactory glomeruli. *Proc. Natl. Acad. Sci. U S A* 108, 18442–18446.
- Saab, A.S., Neumeyer, A., Jahn, H.M., Cupido, A., Simek, A.A.M., Boele, H.-J., Scheller, A., Le Meur, K., Gotz, M., Monyer, H., et al. (2012). Bergmann glial AMPA receptors are required for fine motor coordination. *Science* 337, 749–753.
- Sakadžić, S., Mandeville, E.T., Gagnon, L., Musacchia, J.J., Yaseen, M.A., Yucel, M.A., Lefebvre, J., Lesage, F., Dale, A.M., Eikermann-Haerter, K., et al. (2014). Large arteriolar component of oxygen delivery implies a safe margin of oxygen supply to cerebral tissue. *Nat. Commun.* 5, 5734.
- Sambamoorthy, G., and Raman, K. (2018). Understanding the evolution of functional redundancy in metabolic networks. *Bioinformatics* 34, i981–i987.
- Santello, M., Cali, C., and Bezzi, P. (2012). Gliotransmission and the Tripartite Synapse (Springer), pp. 307–331.
- Santello, M., Toni, N., and Volterra, A. (2019). Astrocyte function from information processing to cognition and cognitive impairment. *Nat. Neurosci.* 22, 154–166.
- Schmid, F., Barrett, M.J.P., Jenny, P., and Weber, B. (2019). Vascular density and distribution in neocortex. *Neuroimage* 197, 792–805.
- Schneider, C.A., Rasband, W.S., and Eliceiri, K.W. (2012). NIH Image to ImageJ: 25 years of image analysis. *Nat. Methods* 9, 671–675.
- Shaw, K., Bell, L., Boyd, K., Grijseels, D.M., Clarke, D., Bonnar, O., Crombag, H.S., and Hall, C.N. (2021). Neurovascular coupling and oxygenation are decreased in hippocampus compared to neocortex because of microvascular differences. *Nat. Commun.* 12, 1–16.
- Shih, A.Y., Blinder, P., Tsai, P.S., Friedman, B., Stanley, G., Lyden, P.D., and Kleinfeld, D. (2013). The smallest stroke: occlusion of one penetrating vessel leads to infarction and a cognitive deficit. *Nat. Neurosci.* 16, 55–63.
- Simard, M., Arcuino, G., Takano, T., Liu, Q.S., and Nedergaard, M. (2003). Signaling at the gliovascular interface. *J. Neurosci.* 23, 9254–9262.
- Srinivasan, R., Lu, T.-Y.Y., Chai, H., Xu, J., Huang, B.S., Golshani, P., Coppola, G., and Khakh, B.S. (2016). New transgenic mouse lines for selectively targeting astrocytes and studying calcium signals in astrocyte processes *in situ* and *in vivo*. *Neuron* 92, 1181–1195.
- Sun, J., Lee, S.J., Wu, L., Sarntinoranont, M., and Xie, H. (2012). Refractive index measurement of acute rat brain tissue slices using optical coherence tomography. *Opt. Express* 20, 1084.
- Theis, M., Söhl, G., Eiberger, J., and Willecke, K. (2005). Emerging complexities in identity and function of glial connexins. *Trends Neurosci.* 28, 188–195.
- Todorov, M.I., Paetzold, J.C., Schoppe, O., Tetteh, G., Shit, S., Efremov, V., Todorov-Völgyi, K., Düring, M., Dichgans, M., Piraud, M., et al. (2020). Machine learning analysis of whole mouse brain vasculature. *Nat. Methods* 17, 442–449.
- Tsai, P.S., Kaufhold, J.P., Blinder, P., Friedman, B., Drew, P.J., Karten, H.J., Lyden, P.D., and Kleinfeld, D. (2009). Correlations of neuronal and microvascular densities in murine cortex revealed by direct counting and colocalization of nuclei and vessels. *J. Neurosci.* 29, 14553–14570.
- Wagner, A. (2005). Robustness, evolvability, and neutrality. *FEBS Lett.* 579, 1772–1778.
- Wallraff, A., Köhling, R., Heinemann, U., Theis, M., Willecke, K., and Steinhäuser, C. (2006). The impact of astrocytic gap junctional coupling on potassium buffering in the hippocampus. *J. Neurosci.* 26, 5438–5447.
- van der Walt, S., Schönberger, J.L., Nunez-Iglesias, J., Boulogne, F., Warner, J.D., Yager, N., Gouillart, E., and Yu, T.; scikit-image contributors (2014). scikit-image: image processing in Python. *PeerJ* 2, e453.
- Weber, B., Keller, A.L., Reichold, J., and Logothetis, N.K. (2008). The microvascular system of the striate and extrastriate visual cortex of the macaque. *Cereb. Cortex* 18, 2318–2330.
- Zack, G.W., Rogers, W.E., and Latt, S.A. (1977). Automatic measurement of sister chromatid exchange frequency. *J. Histochem. Cytochem.* 25, 741–753.
- Zhang, X., Yin, X., Zhang, J., Li, A., Gong, H., Luo, Q., Zhang, H., Gao, Z., and Jiang, H. (2019). High-resolution mapping of brain vasculature and its impairment in the hippocampus of Alzheimer's disease mice. *Natl. Sci. Rev.* 6, 1223–1238.
- Zisis, E., Keller, D., Kanari, L., Arnaudon, A., Gevaert, M., Delemontex, T., Coste, B., Foni, A., Abdellah, M., Cali, C., et al. (2021). Digital reconstruction of the neuro-glia-vascular architecture. *Cereb. Cortex* 31, 5686–5703.
- Zuend, M., Saab, A.S., Wyss, M.T., Ferrari, K.D., Hösl, L., Looser, Z.J., Stobart, J.L., Duran, J., Guinovart, J.J., Barros, L.F., et al. (2020). Arousal-induced cortical activity triggers lactate release from astrocytes. *Nat. Metab.* 2, 179–191.

STAR★METHODS

KEY RESOURCES TABLE

REAGENT or RESOURCE	SOURCE	IDENTIFIER
Antibodies		
chicken polyclonal anti-GFP (1:1000)	Aves	Cat#GFP-1020; RRID:AB_10000240
rabbit polyclonal anti-CollagenIV (1:700)	BioRad	Cat#2150-1470, RRID: AB_2082660
Alexa Fluor 488-AffiniPure donkey anti-chicken IgY (IgG), H + L (1:700)	Jackson ImmunoResearch	Cat#703-545-155, RRID:AB_2340375
Cy3-AffiniPure donkey anti-rabbit IgG, H + L	Jackson ImmunoResearch	Cat#711-165-152, RRID: AB_2307443
DAPI	ThermoFisher	Cat#AG325, RRID: AB_2307445
Bacterial and virus strains		
AAV5-GFAP-mCherry-Cre (titer: 4.0×10^{12} VG/mL)	VVF, UZH Zurich	Cat#v103
AAV8-CAG-Flex-tdTomato (titer: 4.0×10^{12} VG/mL)	VVF, UZH Zurich	Cat#v131
AAV9-GFAP-GCaMP6s (titer: 3.2×10^{13} VG/mL)	VVF, UZH Zurich	Cat#v207
Chemicals, peptides, and recombinant proteins		
tamoxifen (50 mg/kg body weight; stock conc.: 10 mg/mL)	Sigma-Aldrich	Cat#T5648
Isoflurane	Piramal Healthcare	AttaneTM
Texas Red Dextrane 70 kDa (2.5% in NaCl)	Life Technologies	Cat#D-1864
PBS (10X Dulbecco's)-Powder	Axon Lab	Cat#10020938
PFA, Paraformaldehyde Granular	Electron Microscopy Sciences	Cat#19210
donkey serum	abcam	AB7475
Dako Fluorescent mounting medium	Dako	Cat#S3023
Tetric EvoFlow, Ivoclar Vivadent	Dema Dent AG	Cat#398594
fast curing optical adhesive	Thorlabs	Cat#NOA81
Experimental models: Organisms/strains		
ROSA26-floxed-STOP-GCaMP6s (Ai96)	Jackson Laboratory	Madisen et al., 2015 ; Cat#JAX:024106; RRID:AB_1854211
ALDH1L1 CreERT2/+	Jackson Laboratory	Srinivasan et al., 2016 ; Cat#JAX:031008; RRID:IMSR_JAX:031008
Cldn5(BAC)-GFP	Honkura et al., 2018	Honkura et al., 2018
C57BL/6J (JAX™ mice strain)	Charles River	strain code: 632
Software and algorithms		
GraphPad Prism, version V9.1.1.225	GraphPad Software	RRID:SCR_002798
Matlab, version R2020a	MathWorks	RRID:SCR_001622
ImageJ, Fiji version 2.0.0-rc-69/1.52	http://ImageJ.nih.gov/ij	RRID:SCR_003070
ScanImage, version R3.8.1	Janelia Research Campus	RRID:SCR_014307
ZEN blue Software, version 2.6	Zeiss	RRID:SCR_013672
Python, Version 3.7.4	Python	RRID:SCR_008394
Imaris, Version 9.8	Oxford Instruments	RRID:SCR_007370
Deposited data		
ImageJ macro for analysis of vessel density in immunohistological sections	This paper	https://data.mendeley.com/datasets/9gxkf75hdf/1 , https://doi.org/10.17632/9gxkf75hdf.1
Code for measuring astrocyte volume (<i>in vivo</i> data)	This paper	https://data.mendeley.com/datasets/9gxkf75hdf/1 , https://doi.org/10.17632/9gxkf75hdf.1
Code for measuring astrocyte-vessel contact area, volume surface, and astrocyte volume	This paper	https://data.mendeley.com/datasets/9gxkf75hdf/1 , https://doi.org/10.17632/9gxkf75hdf.1
Code for 3D reconstruction of astrocyte-vessel interaction	This paper	https://data.mendeley.com/datasets/9gxkf75hdf/1 , https://doi.org/10.17632/9gxkf75hdf.1

(Continued on next page)

Continued

REAGENT or RESOURCE	SOURCE	IDENTIFIER
Other		
Sapphire glass windows: c-plane sapphire	Hebo Special Glass	Cat#19395-1
Micropism	OptoSigma	Cat#RPB3-01-8-550
Hamilton syringe	Hamilton	Cat#7803-04

RESOURCE AVAILABILITY

Lead contact

Further information and requests for resources and reagents should be directed to and will be fulfilled by the lead contact, Bruno Weber (bweber@pharma.uzh.ch).

Materials availability

This study did not generate new unique reagents.

Data and code accessibility

- All data reported in this paper will be shared by the [lead contact](#) upon request.
- All original code has been deposited at <https://data.mendeley.com/datasets/9gxkf75hdf/1> and is publicly available as of the date of publication. DOIs are listed in the [key resources table](#).
- Any additional information required to reanalyze the data reported in this paper is available from the [lead contact](#) upon request.

EXPERIMENTAL MODEL AND SUBJECT DETAILS

For *in vivo* imaging C57BL/6JA (Charles River) mice and transgenic mice expressing enhanced green fluorescent protein (eGFP) under the Claudin-5 promotor (Cldn5(BAC)-GFP mice; [Honkura et al., 2018](#)) were used for viral intracortical (~P180) and intraventricular (P2) injections. Only female mice were used for viral injections. For the immunohistological analysis ALDH1L1^{CreERT2/+}; ROSA26-floxed-STOP-GCaMP6s (Ai96) mice, were generated by crossbreeding mice expressing the tamoxifen-sensitive Cre recombinase CreERT2 under the control of ALDH1L1 promotor ([Srinivasan et al., 2016](#)) with ROSA26-floxed-STOP-GCaMP6s (Ai96) reporter mice ([Madisen et al., 2015](#); JAX: 024106). For tamoxifen-induced sparse labeling, adult mice (3–6 months) of either sex were used. The primer sequences used for genotyping were as following for ALDH1L1-CreERT2 5'-CTTCAACAGGTGCCTTCCA-3' and 5'-GGCAAACGGACAGAACAGCA-3'; for floxed-STOP-GCaMP6s 5'-ACGAGTCGGATCTCCCTTG-3' and 5'-AAGGGAGCTGCAGTG GAGTA-3' and 5'-CCGAAAATCTGTGGGAAGTC-3' and for Cldn5(BAC)-GFP 5'-CGGCGAGCTGCACGCTGCGTCCTC-3' and 5'-CCTACGGCGTGCAGTGCTTCAGC-3'. Mice group-housed and kept on an inverted 12/12 hr light/dark cycle in standardized cages with food and water ad libitum. All experimental procedures were approved by the local veterinary authorities according to the guidelines of the Swiss Animal Protection Law, Veterinary Office, Canton Zurich (Animal Welfare Act, 16 December 2005 and Animal Welfare Ordinance, 23 April 2008).

METHOD DETAILS

Tamoxifen treatment

Tamoxifen treatment was adapted for sparse labeling from a protocol previously reported ([Saab et al., 2012](#)). ALDH1L1^{CreERT2/+}; ROSA26-floxed-STOP-GCaMP6s (Ai96) mice received one single intraperitoneal (i.p.) injection of tamoxifen at a dose of 50 mg/kg body weight. For quantification of hippocampal astrocytes, a single i.p. injection of tamoxifen at a dose of 100 mg/kg body weight was administered, because the low dose of 50 mg/kg body weight rendered too sparse labeling in the hippocampus. Tamoxifen solution (5 mg/mL or 10 mg/mL dissolved in corn oil) was always freshly prepared for each experimental cohort. Injections were performed in mice at the ages of 8–10 weeks. Experiments were executed 5 days post tamoxifen treatment.

Intraventricular viral injections in pups

C57BL/6 and Cldn5(BAC)-GFP pups were used for unilateral viral injections into the lateral ventricle at post-natal day 2 (P2; [Kim et al., 2013](#)). P2 pups were anaesthetized with isoflurane (1.5–2% in 100% oxygen, flow rate 0.5–1 L/min). 2 µL viral solution per lateral ventricle was injected using a 10 µL 32-gauge syringe (7803-04; Hamilton). Interventricular virus injection is performed 1 mm from the lateral to sagittal suture and halfway between Bregma in a depth of 3 mm. The needle was inserted perpendicular to the skin surface. Viruses used for the experiments were AAV5-GFAP-mCherry-Cre (titer 4.0×10^{12} VG/mL) together with AAV8-CAG-Flex-tdTomato (titer 2.9×10^{12} VG/mL) 2-times diluted in Cldn5(BAC)-GFP or AAV9-GFAP-GCaMP6s (titer 3.2×10^{13} VG/mL) in

C57BL/6 mice. The injected pups were placed back in their home cage after waking up from anesthesia. The mice were housed under normal conditions until 12–15 weeks of age.

Cranial window and intracortical viral injections

Surgical interventions were performed at age 10–15 weeks on two separate days. On the first day, the animals were anesthetized with isoflurane 1.5–2.0% in a mixture of O₂ and air (30/70%) at a flow rate of 400 mL/min. Animals were fixed in a stereotaxic frame (Model 900; David Kopf Instruments) for the head-post implantation as previously described by others (Zuend et al., 2020). In short, fur from the head and neck area was removed a 2 cm long midline incision was made between the eyes to the neck. A bonding agent (Gluma Comfort; Heraeus Kulzer) was applied after cleaning the skull and carefully separating the temporal muscle. Next, a head-cap was formed, made of multiple layers of light-curing dental cement (398594, Dema Dent AG). Finally, a custom-made aluminum head-post was attached. On the second day, a craniotomy was performed using a dental drill (OSSEODOC; Bien-Air), above the left somatosensory cortex, for intracortical virus injection. Animals were anesthetized with a mixture of fentanyl (0.05 mg/kg bodyweight; Sintenyl; Sintetica), midazolam (5 mg/kg bodyweight; Dormicum; Roche), and medetomidine (0.5 mg/kg bodyweight; Domitor; Orion Pharma) injected intraperitoneally, and anesthesia was maintained with midazolam after 50 min (5 mg/kg bodyweight; subcutaneous). Transfection was performed by co-injecting different dilutions of AAV5-GFAP-mCherry-Cre (titer 4.0×10^{12} VG/mL) mixed with AAV8-CAG-Flex-tdTomato (titer 2.9×10^{13} VG/mL) in Cldn5(BAC)-GFP mice. Astrocyte-specific sparse labelling was achieved by injecting the virus mix with 50-, 100-, 200- or 400-times dilution in the respective loci. Injections were performed via a glass capillary to a cortical depth of 300 μ m through the intact dura. For later chronic optical measurements, a square sapphire glass (3 × 3 mm; 19395-1, Hebo Special Glass) was gently placed on the dura mater and sealed with light-curing dental cement (398594, Dema Dent AG).

Microprism implantation

The microprism consists of 1-mm, BK7 glass right-angle prism with an enhanced silver reflective coating (>97.5% reflectivity from 400 to 2000 nm) on the hypotenuse for internal reflection (RPB3-01-8-550; OptoSigma). This allows the raster-scanning pattern of the excitation laser to be translated from an x-y-plane to an x-z-plane. For chronic implantation of the microprism into the mouse cortex a craniotomy was performed as described above. Additionally, the dura was carefully removed. The location of implantation was chosen to cause minimal disruption of surface blood vessels. With a small sucking tip (0.4 mm; 634847; Ivoclar Vivadent) brain tissue was removed where the prism would be implanted. The tissue was continuously washed with Ringer's solution (135 mM NaCl, 5 mM KCl, 5 mM HEPES, 1.8 mM CaCl₂, 1 mM MgCl₂) until bleeding stopped. For stable chronic imaging the microprism was glued (NOA81, Thorlabs) to a square sapphire glass (3 × 3 mm; 19395-1, Hebo Special Glass) and cured with blue light (Superlight I 05, Lumatec). The microprism was held with a custom-made holder for precise insertion of the microprism into the brain. The craniotomy was then sealed with light-curing dental cement (398594, Dema Dent AG). Imaging was performed 4–6 weeks after window implantation.

Fluorescence check

Three weeks after injection the animals were checked for sensor expression. Excitation light was delivered at 510 nm for an overview of the vessel structure, 490 nm for the excitation of and 600 nm for the excitation of TdTomato by a monochromatic-based illumination system (Polychrome V; Till Photonics). Fluorescence was collected with a fluorescence stereo microscope (Leica MZ16FA with a Planapo 1.0× objective; Meyer Instruments). Vessel images were recorded with a high-performance digital CCD camera system (Pixelfly; PCO) with an exposure time of 50 ms for the vessel images and 500 ms for fluorescence images. We used emission filters for yellow and green (F47-535; AHF Analysentechnik), and red (F47-623; AHF Analysentechnik) to detect fluorescence emission. Image acquisition was controlled by Camware software (V3.09; PCO). Vessels imagines and fluorescent maps were combined to determine the location of the expression site in respect to the vessel structure.

Visualization of blood plasma during imaging

40 μ L of Texas red dextran (70 kDa; D1864; thermo fisher scientific) 2.5% in NaCl were intravenously (i.v.) injected for the visualization of the blood plasma during imaging. For intravenous injections, a 30 Gauge needle was connected to fine bore polyethylene tubing (0.28 mm ID; 0.61 mm OD; Portex; Smith medical), filled with 0.9% saline solution and inserted into one of the tail veins.

Microscope design and *in vivo* imaging parameters

A custom-made two-photon laser scanning microscope (Mayrhofer et al., 2015) equipped with a two-photon laser with <120 fs temporal pulse width (InSight DeepSee Dual; Spectra-Physics) was used for image acquisition. Conventional two-photon imaging was performed with a 20x water immersion objective (Objective W Plan-Apochromat 20x/1.0 DIC; Zeiss). Imaging through a prism was performed with 16x water immersion objective (CFI75 LWD 16X W; Nikon). For adjustments in the nanometer range of the focal plane along the Z-direction, the objective was mounted to an additional piezo motor-driven linear stage with 800 μ m travel range and a precision of 1.8 nm (P-628.1CD; Physik Instrumente). A notch filter (F78-064; AHF-Analysentechnik) was used for beam overlay and alignment of both beams. Excitation and emission beam paths were separated by a dichroic mirror (F73-825; AHF Analysentechnik). A dichroic mirror at 506 nm (F38-506; AHF Analysentechnik) and 560 nm (F38-560; AHF Analysentechnik)

separated the emission light beam. The emission light was focused on the photomultiplier (H9305-03, Hamamatsu) by two lenses (LA1050-A1 and AL5040-A2; Thorlabs). We used emission filters for blue (F39-477; AHF Analysetechnik), green and yellow (F37-545; AHF Analysetechnik) and red (F39-608; AHF Analysetechnik) for multi-color imaging. ScanImage (Pologruto et al., 2003; RRID:SCR_014307). Anatomical imaging was performed at a resolution of 512 × 512 pixels at a frequency of 0.74 Hz. GCaMP6s, eGFP and Texas red dextran were excited with 940 nm. Red labeled astrocytes (mCheery/tdTomato) were excited with 1040 nm. The cortical layers were defined as follows: layer I – 0–100 μm; layer II/III – 100–250 μm; layer IV – 250–350 μm; layer V – 350–500 μm.

Pixel size calibration

For pixel size calibration 4 μm beads (T7283; Thermo Scientific) were mounted on a SuperFrost Plus slide (Thermo Scientific). The sample was sealed using a 0.17 mm cover glass and nail polish. The slide was mounted on a slide holder (MAX3SLH; Thorlabs) that was mounted on a linear micrometer stage (MBT402; Thorlabs) for lateral micrometer precision manipulations in x- and y-coordinates of the microscope. Lateral movements were measured with a micrometer watch attached to the linear stage (CA801346; Käfer). The stepper motors controlling the large movements of the microscope body were deactivated during the measurements to avoid residual vibrations which would have slightly distorted the images.

PSF measurements and deconvolution

To measure the point spread function (PSF), sub-micron fluorescent beads 175 nm in diameter (P7220; ThermoFischer) were used to approximate a fluorescent point source of the two-photon microscope. Fluorescent beads were acquired from the green and red channels to establish channel specific PSF. To estimate the PSF, we used a chamber at defined thicknesses to simulate image acquisitions at different depths of the brain. First, the fluorescent beads were mounted on a SuperFrost Plus slide (Thermo Scientific). The sample was sealed using a 0.17 mm cover glass and nail polish to ensure a stable preparation. Second, the chamber was mounted on top of the slice consisting of a metal disk at a defined thickness (50, 100, 300, 500 and 1000 μm) with a hole in the center forming a small well (3 × 3 mm). Next, the well was filled with glycerol solution designed to mimic the refractive index of the gray matter of the cortex (Rosas et al., 2017; Sun et al., 2012). At last, a sapphire glass (3.5 × 3.5 mm; 19395-1, Hebo Special Glass) was placed on top of the metal disk and sealed with silicon glue (Xantopren Comfort light; Kulzer). A diagram of this chamber is provided in Figures S2A and S2B. The slide and the sealed chamber were mounted on a slide holder (MAX3SLH; Thorlabs). The stepper motors controlling the large movements of the microscope body were deactivated during the measurements to avoid residual vibrations which would have slightly distorted the images. Slice-to-slice steps were set to 250 nm. In average 41.5 ± 14.5 PSFs were collected for each objective (16x and 20x) and from each depth condition with a mean power of 23.1 ± 9.1 mW. Collected PSFs were analyzed with Huygens Professional PSF Distiller version 20.04 (RRID:SCR_014237; Scientific Volume Imaging; the Netherlands; <http://svi.nl>), using the CMLE algorithm, with SNR 40 iterations.

Immunohistology

Tamoxifen-injected ALDH1L1CreERT2/+; ROSA26-floxed-STOP-GCaMP6s (Ai96) mice were used for immunohistology. Mice were anesthetized with pentobarbital and transcardially perfused with 20 mL ice-cold phosphate-buffered saline (PBS, pH 7.4, (10X Dulbecco's)-Powder, Axon Lab AG, Baden-Dättwil, Switzerland) followed by 60 mL ice-cold 2% paraformaldehyde (PFA, Paraformaldehyde Granular, Electron Microscopy Sciences, Hatfield, PA) in PBS (pH 7.4) with a flow of 20 mL/min. Brains were dissected, halved sagittally and post-fixed in 4% PFA for 3 hr at 4°C. Tissue was cryoprotected in 30% sucrose in PBS for ≈24 hr at 4°C, and then stored at -80°C until cutting. Sagittal sections (40 μm) were cut using a microtome (Hyrax KS 34) and then stored in anti-freeze solution (50 mM sodium phosphate buffer pH 7.4, 1 M glucose, 35% ethylene glycol and 3.5 mM sodium azide) at -20°C until further processing. Free floating sections were preblocked in 0.3% Triton X-100 (Sigma-Aldrich, Buchs, Switzerland) in Tris buffer (50 mM, pH 7.4) and 5% donkey serum (blocking solution) for 1 hr at room temperature (RT). Sections were then incubated with primary antibodies chicken anti-GFP (Aves, Cat: GFP-1020, RRID:AB_10000240, 1:1000) and rabbit anti-CollagenIV (BioRad, Cat: 2150-1470, RRID: AB_2082660, 1:700) diluted in blocking solution overnight at 4°C. Then, sections were incubated in Alexa Fluor 488-AffiniPure donkey anti-chicken IgY (IgG) (H + L, Jackson ImmunoResearch, Cat: 703-545-155, RRID:AB_2340375, 1:700) and Cy3-AffiniPure donkey anti-rabbit IgG (H + L, Jackson ImmunoResearch, Cat: 711-165-152, RRID: AB_2307443, 1:700) secondary antibodies for 45 min at RT. For nuclei labeling, DAPI (ThermoFisher, Cat: AG325, RRID: AB_2307445, stock solution: 1 mg/mL; use 1:10000) was added to the secondary antibody solution. Sections were mounted on SuperFrost Plus slides (Thermo Scientific) in Dako Fluorescence Mounting Medium (Dako, Jena, Germany).

Image acquisition of histological preparations

Confocal images were acquired using a Zeiss LSM 800 confocal laser scanning microscope equipped with a 10x (Plan-Apochromat, NA 0.45), a 25x (LCI Plan-Neofluar, NA 0.8) or a 40x objective (Plan-Apochromat, NA 1.4, Oil DIC (UV) VIS-IR). Overview pictures of the whole sagittal sections were taken using the 10x objective and the tile scan option of the built-in microscope software (RRID:SCR_013672; ZEN software, Zeiss). Z-stacks of every single astrocyte was taken using the 40x objective with an interval of 1.5 μm. Confocal images present single plane tile scans and maximum intensity projections of z-stacks.

Astrocyte size analysis and astrocyte properties

To compute the volume of astrocytes imaged *in vivo* and compare the size of astrocytes between brain regions from immunohistochemical preparations, a z-projection of the image stack was taken in the imaging plane (XY) and the orthogonal planes (XZ and YZ). The astrocyte was manually circled in each plane in ImageJ (Fiji, Version 2.0.0-rc-69/1.52; RRID:SCR_003070; [Girish and Vijayalakshmi, 2004](#); [Schneider et al., 2012](#); see also [Figure S3A](#)) to determine the size and shape of the astrocyte. The manually circled domains were imported (*ReadImageJROI*) and further analyzed in MATLAB R2020a (RRID:SCR_001622; MathWorks) with the function *polyshape* to compute the astrocyte area and the axial properties of the manually circled polygon (*alphaShape* and *criticalAlpha*). The elliptic fit was computed with the function *fit_ellipse*. The astrocytic volume was computed from the manually circled domains of each plane (XY, XZ and YZ) with the minimum volume enclosing ellipsoid function *MinVolEllipse* in MATLAB. To count the number of vessels contacted by an astrocyte, image stacks were visually inspected. For analysis of astrocyte-vessel interactions the part of the vasculature that connects two bifurcations was counted as one vessel (see also [Figure 3C](#); Hippocampus). To analyze layer dependent astrocyte sizes and vessel interactions, astrocytes were sorted by cortical depth measured from the brain surface. The cortical layers were defined as follows: layer I – 0–100 µm; layer II/III – 100–250 µm; layer IV – 250–350 µm; layer V – 350–500 µm.

Correlation analysis and 3D visualization

For quantitative analysis of astrocyte-vessel interactions only a subset of the *in vivo* imaged astrocytes was used. The selection of astrocytes was based on spatial resolution, signal-to-noise ratio, contrast and fluorescent signal. Out of the 697 cortical stacks of astrocytes and vessels, 106 fulfilled the necessary criteria to perform the computational image analysis. Automatic vessel and astrocyte segmentation was performed by successive thresholding and filtering techniques in Python ([Lee et al., 1994](#); RRID:SCR_008394). First, acquired images were cropped according to the manually drawn ROIs to determine the size of an astrocyte (see paragraph “[Astrocyte size analysis and astrocyte properties](#)” above). Subsequently, each channel was separately segmented to isolate the astrocyte and the vessels separately. Astrocyte and vessel segmentation were performed with the 2D triangle thresholding method ([Zack et al., 1977](#)) implemented in skimage ([van der Walt et al., 2014](#)) by applying it to every slice of the image stack followed by a binary opening operation. For the astrocyte segmentation, the voxels with a fluorescence value higher than the 80th percentile were set to the voxel value at the 80th percentile to prevent extreme voxel values that could skew the following slice-wise 2D Li-thresholding method ([Li and Lee, 1993](#)). To prevent over-segmentation the threshold was set to the mean of the channel if the calculated threshold at a specific slice was lower than the mean of the astrocyte channel. To optimize the astrocyte segmentation, it was assumed that only one cell was visible in an image and thus only the largest connected area was considered. A 3D median filter of 5 was applied to smooth the segmentation. The astrocyte area was obtained by inverting the astrocyte segmentation and convolving the image with a 3 × 3 × 3 voxel 3D convolution filter, where each voxel connects to the face area of the neighboring voxel representing the outer face of the astrocyte. The volume of the astrocyte was calculated by counting the number of voxels of the astrocyte segmentation and multiplying it with the voxel volume. To exclude noisy segmentation patches for the vessel segmentation, a threshold was applied that only connected areas larger than 5000 voxels were considered. The total area of the vessel channel was calculated by inverting and performing the 3D convolution where only voxels at the border of the vessel segmentation were selected. The vessel volume fraction was calculated by dividing the number of voxels in the vessel segmentation by the total images’ voxel number. To obtain the average vessel diameter a 3D median filter of 13 voxels was applied to ensure a smooth segmentation. Smoothness was required for the skeletonization and determination of the vessel center when using the algorithm by ([Lee et al., 1994](#)) implemented in skimage ([van der Walt et al., 2014](#)). To calculate the contact area between vessels and astrocytes, the astrocyte channel was first dilated with a 5 × 5 × 5 voxel structure to ensure vessels close to the astrocyte are defined as contact area. Next, the astrocyte and vessel segmentation were overlayed to identify overlapping areas. Only a connected voxel area >500 was considered as contact area.

3D visualizations, based on the segmented datasets, were further processed using Imaris (Oxford Instruments, Imaris Version 9.8; RRID:SCR_007370). Each slice was stacked and merged to create a 3D model of the astrocyte and vessel channel. Each pixel (x, y and z) was transformed to micrometers for the final visualization of the 3D model calculated from the pixel size calibration (see section [Pixel size calibration](#) above). To evaluate the nature of the contact ([Figure 1A](#), right column), we adjusted the opacity (color type = transparent 0) of each slice in the vessel channel for better visualization of astrocyte-vessel interactions in the final 3D model. For the 3D animation, a camera was added in Imaris to create the entire model for a 360-degree rotation to visualize the entire reconstruction of the astrocyte and vessel structure.

Vessel density of immunohistological section

Vessel density was quantified with ImageJ (Fiji, Version 2.0.0-rc-69/1.52; RRID:SCR_003070; [Girish and Vijayalakshmi, 2004](#); [Schneider et al., 2012](#)). Noise was reduced using the “despeckle” option in ImageJ and a Gaussian blur filter was added with a sigma = 1. Thresholding method was “Huang”, then “Analyze Particles” was used to measure the %area.

QUANTIFICATION AND STATISTICAL ANALYSIS

All statistical details, including the exact value of n, what n represents and which statistical test was performed are listed in [Table S1](#) and can also be found in the figure legends or in the figures. All data plotting and statistical analysis was performed in GraphPad Prism

(RRID:SCR_002798; Version 9.1.1.225). Data is presented as mean \pm SEM. p values < 0.05 were considered statistically significant. Data was visualized in scatter dot plots with mean \pm SEM, or boxplots with the sample median, first and third quartile (box), and the minimum and maximum of the sample (whiskers). All datasets were tested for Gaussian normality using the D'Agostino-Pearson (omnibus K2) normality test. If datasets were normal, one-way ANOVA was used. Post hoc comparisons were corrected using the Tukey method. If normality was rejected, the nonparametric Kruskal-Wallis test was used. Post hoc comparisons were corrected using the Dunn's method. Pearson's linear correlation coefficient with a 95% confidence interval at a significance level of 0.05 was used for correlations analyses. Sample sizes were not determined in advance, since they were constrained by the sparse-labelling protocol efficacy.